Serb. Astron. J. № 211 (2025), 71 - 90
DOI: https://doi.org/10.2298/SAJ250531003N

UDC 523.98 : 004.932 : 52–44
Original scientific paper

HIGH PRECISION AUTOMATIC CORONAL HOLE DETECTION FROM JANUARY 2019 TO JULY 2023 USING THE AIA 193 Å DATA OBTAINED BY SOLAR DYNAMIC OBSERVATORY

Dibyadeep Nandi[1], Soumya Roy[2], Amrita Prasad[3] and Sankar Narayan Patra[1]

[1] *Department of Instrumentation & Electronics Engineering, Jadavpur University, India*
E–mail: *dibyadeep.nandi@gmail.com*

[2] *Department of Applied Electronics & Instrumentation Engineering, Haldia Institute of Technology, MAKAUT, India*

[3] *Department of Data Science, Cardiff School of Technologies, Cardiff Metropolitan University, United Kingdom*

(Received: May 31, 2025; Accepted: July 21, 2025)

SUMMARY: Coronal holes (CHs) play an important role in solar physics. They contribute to geomagnetic storms. The emission of charged particles into interplanetary space influences the space weather. CHs, being an important part of the solar activity, have a significant influence on Earth's climate. So, detection of CH regions is a significant task. Many attempts have already been made in this regard. In this work, we are proposing a new method for automatic detection of CH regions using a deep learning technique. We used Supervised Intensity Thresholding with Distance Transform Clustering and Connected Component Labeling (SITDTCCCL) to find out Regions of Interest (ROI) on 193 Å images collected from the Solar Dynamics Observatory (SDO). The state-of-the-art deep learning method (YOLO v8) has shown excellent performance in detection of CH regions with scores of evaluation matrices such as F1 score 95%, Precision 97.1%, mAP50 98.1%, and True Positive Rate (TPR) 100%.

Key words. Sun: corona – Sun: activity – Sun: magnetic fields – Sun: UV radiation – solar-terrestrial relations – Methods: data analysis – Techniques: image processing

1. INTRODUCTION

Significant solar activities like CHs, coronal mass ejections (CMEs), solar flares, solar prominences, and solar wind have an impactful contribution to the interplanetary magnetic field (IMF) Gosling and Pizzo (1999), Odstrčil and Pizzo (1999), Cranmer (2009) and also affect the Earth in various ways. Therefore, CHs are of great importance to the domain of solar physics Baek et al. (2021). In the years of solar maximum, CMEs contributed greatly to the generation of solar wind, but in the solar minimum phase, CHs become the main source of solar wind. Moreover, CHs can send out the same amount of charged particles as CMEs throughout their lifetime Gopalswamy et al. (2009), Krista and Gallagher (2009).

The corona is the outermost layer of the Sun. CHs are prominent dark patches over the solar corona, apparent on the Atmospheric Imaging Assembly (AIA) images acquired through extreme ultraviolet (EUV) and soft X-ray channels Altschuler et al. (1972), Wang et al. (1996), Antonucci et al. (2004). CHs can occur anywhere on the Sun and persist for several solar rotations. They can often be observed during the waning phase of the solar cycle. Polar coronal holes

tend to be the most common and persistent. Equatorial CHs can occur in isolation over a region or spread out as extensions of polar CHs. Sometimes CHs can spread from pole to pole, but they are infrequent.

Bright regions manifest on the surface of the solar corona where magnetic field lines are generated and form loops. CHs present as dark regions due to the presence of cooler plasma, which is two to three times less dense than the regions of quiet Sun Antonucci et al. (2004), has temperature around $10^5 - 10^6 K$ Wilhelm (2006) and is embedded in open magnetic field Sheeley and Wang (2002), spreading out into the interplanetary space acting as a source of a stream of charged particles called the solar wind Altschuler et al. (1972), Krieger et al. (1973), Hassler et al. (1999), Antonucci et al. (2004), Vršnak et al. (2007). When a rapid outflow of charged particles becomes entangled with Earth's magnetic field, it leads to diverse effects on our planet. This phenomenon adversely affects Earth's magnetic shield, inducing turbulence and altering its shape, potentially gives rise to geomagnetic storms Lakhina and Tsurutani (2016). This process accelerates Earth's atmospheric temperature, and the projected charged particles instigate auroras in polar regions. A thorough statistical investigation of coronal holes (CHs) and a detailed analysis of their physical parameters, such as intensity, area and magnetic polarity are crucial for obtaining a comprehensive understanding of the solar wind dynamics Robbins et al. (2006) and its geomagnetic effects Rotter et al. (2015). Identification of CHs on the solar disk is an inevitable task for astronomical research.

2. RELATED WORKS

The rudimentary work of coronal hole detection was proposed by Harvey and Recely (2002), based on hand-drawn synoptic maps. Henney and Harvey (2007) presented an automated coronal hole detection, an extended version of the work done by Harvey and Recely (2002), by using the Kitt Peak Vacuum Telescope (KPVT) 10830 Å spectroheliograms and photospheric magnetograms with unique formations of the helium lines along with some morphological operations. Recently, various machine learning-based automated methods have been proposed for the identification of CHs. Malanushenko and Jones (2005) proposed the line half-width and central intensity-based differentiation techniques between the coronal holes and the quiet Sun (QS). De Wit (2006) used the Karhunen–Loève transform for singular value decomposition (SVD), used in the multispectral feature vector-based Bayesian classification for identification of large-scale solar objects. De Wit (2006) detected CHs, chromospheric network, and active regions(AR), with a Bayesian classifier-based supervised segmentation scheme. Barra et al. (2009) proposed a region-based and unsupervised multispectral segmentation method using a possibilistic clustering algorithm and a context-dependent fusion operator. Scholl and Habbal (2008) presented an automated differentiation technique between CHs and filaments on (SOHO/EIT) images Delaboudinière et al. (1995) and the Michelson Doppler Imager (SOHO/MDI) images Scherrer et al. (1995). Kirk et al. (2009) introduced a new method of computation named perimeter tracing to estimate the perimeter of a polar coronal hole. Krista and Gallagher (2009) proposed a fast and robust histogram-based intensity thresholding technique for the CH segmentation. Barra et al. (2009) presented a fast and robust segmentation algorithm for identification of CHs, ARs, and QS, which is a modification of the spatial possibilistic clustering algorithm (SPoCA). de Toma (2011) proposed a double thresholding method for identification of large solar objects. Colak and Qahwaji (2013) presented a fuzzy algorithm for segmentation of CHs and ARs from images of the Atmospheric Imaging Assembly (AIA), Lemen et al. (2012), also used Radial Basis Function Networks (RBFNs) introduced by Qahwaji and Colak (2007). Verbeeck et al. (2014) segment out ARs and CHs according to their intensity level using a fuzzy clustering scheme, named SPoCA-suite. Lowder et al. (2017) presented measurements on CHs and open magnetic flux computed by a potential field source surface (PFSS) model on the multiple spectrum. Ciecholewski (2015) used a watershed algorithm to identify CHs. Boucheron et al. (2016) proposed an extraction and characterization method of CHs from images obtained by SDO/AIA using an edgeless active contour algorithm. Caplan et al. (2016) introduced a double-threshold region-growing image segmentation algorithm that was used to identify CHs. Garton et al. (2018) used a new technique of extraction of the CH information called the coronal hole identification via the multi-thermal emission recognition algorithm (CHIMERA) using the multiple pass-bands of AIA and HMI images Scherrer et al. (2012) from SDO Malanushenko and Jones (2005). Illarionov and Tlatov (2018) presented a CNN-based automatic technique of the CH segmentation. Bandyopadhyay et al. (2020) introduced a robust algorithm to segment out the CHs regions by using a Hough transform-inspired fuzzy energy simulated dual contour method. Illarionov et al. (2020) presented a CNN network trained on 193 Å AIA samples of SDO, which is able to segment CHs on solar synoptic maps and polar heliographic projections. Jarolim et al. (2021) acquired multichannel HMI and AIA data of SDO on the entire 24th solar cycle and proposed a CNN-based automatic technique of the CH segmentation, which can determine the CH boundaries with accuracy of 98.1%. Ervin (2021) utilizes two essential machine learning techniques, namely the CNN and K-means clustering to determine the CH regions over the images obtained by EUVI/STEREO A/B (195 Å) and SDO/AIA (193 Å).

"Detection" is a basic problem in computer vision, which stands for the proper identification of ob-

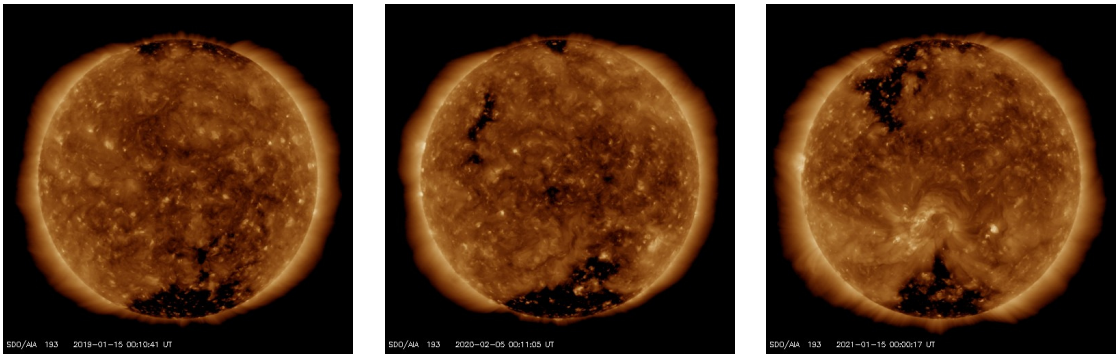

(a) (b) (c)

Fig. 1: (a) 193 Å AIA image with prominent northern and southern polar CHs on 2019/01/15, (b) 193 Å AIA image with visible northern, southern polar CH, a CH near north-western solar limb, and small CH regions on solar equator captured on 2020/02/05, and (c) 193 Å AIA image with elongated and prominent polar CH regions in both northern and southern solar hemisphere captured on 2021/01/15.

jects Huang et al. (2017). In recent studies, many object recognition models have been proposed which comprise the essence of deep learning and convolutional neural networks (CNNs). "You Only Look Once" (YOLO) Redmon et al. (2015) and Single Shot Multi-Box Detector (SSD) Lin et al. (2016) are 1-stage detectors, perform the task of object classification and detection. The Region-based Convolutional Neural Network (R-CNN) incorporates a class-agnostic region proposal module to perform the task. Fast R-CNN Girshick et al. (2014) increases accuracy and speed, due to its simplified training procedure. Faster R-CNN Ren et al. (2017) shows better accuracy than Fast R-CNN. Lin et al. (2017) proposed the Feature Pyramid Network (FPN), which is used to enhance the detection ability of small objects. Mask R-CNN He et al. (2017), Cascade R-CNN Cai and Vasconcelos (2018) and Region-based Fully Convolutional Networks (R-FCN), Dai et al. (2016) are known as 2-stage detectors. The architecture of YOLOv2 Redmon and Farhadi (2017) is framed on Darknet-19 containing 19 convolutional layers. YOLOv3 Redmon and Farhadi (2018) is regarded as a milestone for object detection which performed object detection on the Microsoft COCO dataset Lin et al. (2014). Darknet-53 formed the backbone of YOLOv3. YOLOv4 was presented in Bochkovskiy et al. (2020). YOLOv5 Jocher et al. (2020), the first YOLO model belongs to Ultralytics. It includes an autoanchor algorithm. YOLOv6 Li et al. (2022) consists of RepVGG or CSPStackRepblocks, an efficient hybrid-channel strategy with advanced quantization techniques. A couple of changes were introduced in YOLOv7 Wang et al. (2022), among them, the extended efficient layer aggregation network (E-ELAN) and the planned re-parameterized convolution was notable. YOLOv8 Jocher et al. (2023) came with five scaled versions: YOLOv8n (nano), YOLOv8s (small), YOLOv8m (medium), YOLOv8l (large), and YOLOv8x (extra large). YOLOv8 supports multiple tasks such as object detection, segmentation and classification.

Solar physics has witnessed efforts to detect solar objects such as coronal mass ejections (CMEs), coronal holes (CHs), active regions (ARs), and sunspots. In this experiment, localization of CHs on the 193 Å images of SDO is our main objective. There are several techniques for finding out ROI, i.e. CH regions, such as the intensity thresholding Henney and Harvey (2007), perimeter tracing Kirk et al. (2009), active contour detection Scholl and Habbal (2008), edgeless active contour detection Boucheron et al. (2016), and energy-based active contour detection Bandyopadhyay et al. (2020). Excluding the intensity thresholding method, the rest of the methods are categorized as region-growing techniques. In the existing literature, various studies have utilized the deep learning methods to categorize coronal holes (CH) as a solar event alongside other solar phenomena such as active regions (AR) and solar flares Kucuk et al. (2017a), Armstrong and Fletcher (2019). These studies trained their classification models using cropped images and the output was presented as an image rather than pinpointing the locations of the events on the solar disk. In a distinct approach, Baek et al. (2021) used Single-Shot Multibox Detector (SSD) and Faster Region-based Convolutional Neural Network (Faster R-CNN) to localize coronal hole regions in their investigation of solar event classification. However, it should be noted that the accuracy of these methods was observed to be relatively low. We introduce an automatic coronal hole detection technique using SITDTCCCL with YOLO v8. The novelty of our work lies in the following aspects: the primary challenge in intensity thresholding is the selection of an appropriate threshold value, and the time-consuming nature of the two-stage contour computation using the fuzzy energy-based ac-

tive contour method. To address this trade-off we propose a novel approach known as Supervised Intensity Thresholding with Distance Transform Clustering and Connected Component Labeling (SITDTC-CCL). This method integrates the benefits of both the intensity thresholding and region-growing techniques, and it is presenting a solution that has not been explored in the domain of solar physics. This innovative approach aims to eliminate the drawbacks associated with the threshold value determination and contour computation time, and offers a more efficient and effective alternative. We use more advanced object detection algorithms (YOLO v8n, YOLO v8m, YOLO v8x) for localization of the CH regions, and achieve higher accuracy in detection of the CH regions.

3. DATA SOURCE

3.1. Solar Dynamics Observatory (SDO)

SDO Pesnell et al. (2012) is a part of NASA's Living With a Star (LWS) mission, launched in 2010. The Atmospheric Imaging Assembly (AIA) Lemen et al. (2012), the Helioseismic and Magnetic Imager (HMI) Schou et al. (2012) and the Extreme Ultraviolet (EUV) Variability Experiment (EVE) Woods et al. (2012) are three scientific instruments incorporated with SDO. AIA aimed to provide an unprecedented view of the heliosphere, taking images that span at least 1.3 solar diameters in multiple wavelengths (94 Å, 131 Å, 171 Å, 193 Å, 211 Å, 304 Å, 335 Å, 1600 Å, 1700 Å, and 4500 Å) every 12 seconds Lemen et al. (2012) at a resolution of about 1 arcsecond. The HMI instrument is designed to measure the Sun's internal magnetic oscillations and the magnetic field at the photosphere, providing magnetograms and intensitygrams with time cadences of 45 s and 720 s, respectively. The entire solar disk is captured by HMI at 6173 Å with a resolution of 1 arcsecond. AIA and HMI produce images of various resolutions, 4096 × 4096, 2048 × 2048, 1024 × 1024, 512 × 512, and 256 × 256 pixels, and daily generate 1.5 TB of data. The total data size from SDO to date is approximately 5 PB. This enormous data set generated by SDO contributed to eclectic studies and the application of deep learning techniques in solar physics Kucuk et al. (2017b), Armstrong and Fletcher (2019). We use the SDO/AIA data to train the CH auto-detection models.

3.2. Data acquisition

For this experiment, we have used 193 Å images with resolution 512 × 512, obtained from the Solar Dynamic Observatory (SDO) Pesnell et al. (2012) (https://sdo.gsfc.nasa.gov/data/), for the period of 4 years and 7 months, starting from 1 January 2019 to 31 July 2023. We have acquired data between the ending phase of the 24th solar cycle and the starting phase of the 25th solar cycle. We worked with images of size 512 × 512 because the maximum image size supported by Yolo is 640x640, and we want to avoid any preprocessing of those used images. SDO captures 7200 full disk images of a specific channel or wavelength every day. From this huge number of images we have taken one sample per day Krista and Gallagher (2009), Bandyopadhyay et al. (2020). The solar disk of the AIA 193 Å channel is apparently in a brown shade. In the EUV image, the white regions represent hot flare plasma, ARs, and CMEs and dark patches on the photosphere represent the CH regions. Though the solar cycle 25 started on December 2019, we collected the data from 1 January 2019 as we wanted to use more than 1500 images for this work. In this course of data acquisition, the separation of the corrupted image from the full disk image was the main challenge. We created a full-disk CH data set from AIA 193 Å images by resolving the data preparation challenge manually, a process that was time-consuming and required almost eight hours.

4. PROPOSED METHOD

We used the 193Å image channel as an input in the system and converted the image into a grayscale image using the mean value of three channels of the colour image, which can be expressed in the following Eq. (1).

$$L = \frac{1}{n}\sum_{i=1}^{n} I_i\,(x, y)\,. \tag{1}$$

After converting the image into grayscale, the subsequent step involves the solar disk segmentation. To achieve this, we generated a mask with coordinates corresponding to the solar disk, effectively masking the background while preserving the solar disk. Traditional intensity thresholding methods as proposed by Henney and Harvey (2007), Krista and Gallagher (2009), typically involve the trial-and-error selection of an initial threshold. In contrast, de Toma (2011) used a two-stage thresholding technique for the detection of coronal hole regions. The first threshold was utilized to separate ARs from the image, and the second threshold was applied to distinguish the CH regions from the quiet Sun.

We aim to determine an effective threshold for the CH region detection by evaluating initial threshold values derived from a set of images. S is a set of randomly selected grayscale samples of the 193 Å data, where we selected one sample randomly from the data points of the entire month on the period starting from January 2019 to July 2023, and S_{GTH} is the set of respective CH maps of SWPC. I_{Gray} and I_{TH}, a grayscale data, and its corresponding ground truth. Localization of CHs on the 193 Å image, initially done by visual identification with the aid of the ground truth. We use the impixelinfo(x, y) function, which offers pixel-wise insight into the

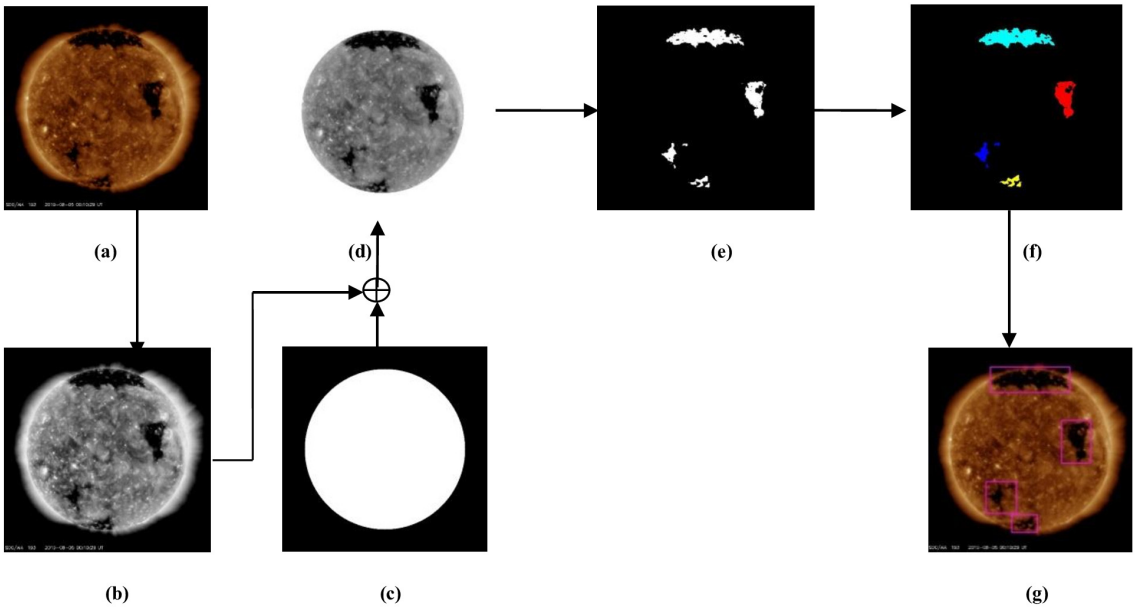

Fig. 2: Steps of ROI detection. (a) An AIA 193 Å image, (b) Converted Gray Scale image, (c) Mask Image of Image (b) for solar disk segmentation, (d) Segmented Solar Disk, (e) Supervised Thresholding, (f) Distance Transform Clustering(DTC) and Connected Component Labeling, (g) Detected ROI (CH regions).

Input: Set of gray scale solar image **S** of size n
Input: Set of ground truth of solar image S_{GTh} of size n
Output: Selected threshold τ
for $i = 1$ *to* n **do**
  $I_{Gray} \in S$
  $I_{Th} \in S_{GTh}$
  $L^i_{max} = max\_CH\_intensity\,(I_{Gray}, I_{Th})$
  $L^i_{min} = min\_CH\_intensity\,(I_{Gray}, I_{Th})$
end
$Lb_R = min\left(L^i_{min}\right)$
$Ub_R = max\left(L^i_{max}\right)$
for $i = 1$ *to* n **do**
  for $k = Lb_R$ *to* Ub_R **do**
    $[I_B] = gray2bin\,(I_{Gray}, k)$
    $[F_k] = max\_accuracy\,(I_B, I_{Th})$
  end
  $\left[F^i_{max}\right] = find\_max\,(F_k)$
end
τ =mean$\left(F^i_{max}\right)$

Algorithm 1: Supervised threshold selection algorithm.

CH regions. The enlisted maximum and minimum threshold intensity of the CH regions helps to determine the upper limit and the lower limit of threshold intensity. For every sample of S, binarize the grayscale image for every threshold intensity, starting from Lb_R to Ub_R, by incrementing the threshold value by one. Accuracy of binary samples is checked against the ground truth. In this study, we used the percentage of the CH regions on the solar disk Bandyopadhyay et al. (2020) as an accuracy measure. Threshold acquired the highest accuracy and is enlisted into F^i_{max}. The mean value of all data points on F^i_{max} is the supervised threshold intensity τ. Subsequently, we applied Distance Transform Clustering (DTC) Starovoitov (1996) in the next step to group the nearby regions together. The algorithm operates as follows:

Step 1: Selection of discretization parameter:
ω is a set of M observation in the feature space of n dimensions. From the set of input observation, PT cluster cores will be identified. Let $f : R_n \to Z_n$, map ω into discrete space Z^n, a point in Z^n will be identified with label l if the respective hypercube contains one observation, denoted as ω_D. Find t_l, varying the chosen function $K_l = (\phi_l)$ and using PT2 on the basis of the metric.

Step 2: Data discretization:
Continue with the discritization with the parameter t_l.

Step 3: Core extraction:
There exist two variants for the two corresponding filters $PT1$ and $PT2$. The filter with the variant $PT1$ can be used for a) erosion, b) opening, c) dilation followed by opening, d) opening followed by closing. All the equations related to this step are given in Eq. (2) - Eq. (5):

$$\varphi_1 = PT1^+_{\text{th}}\,(Z^n) \equiv \Omega^D \ominus R, \tag{2}$$

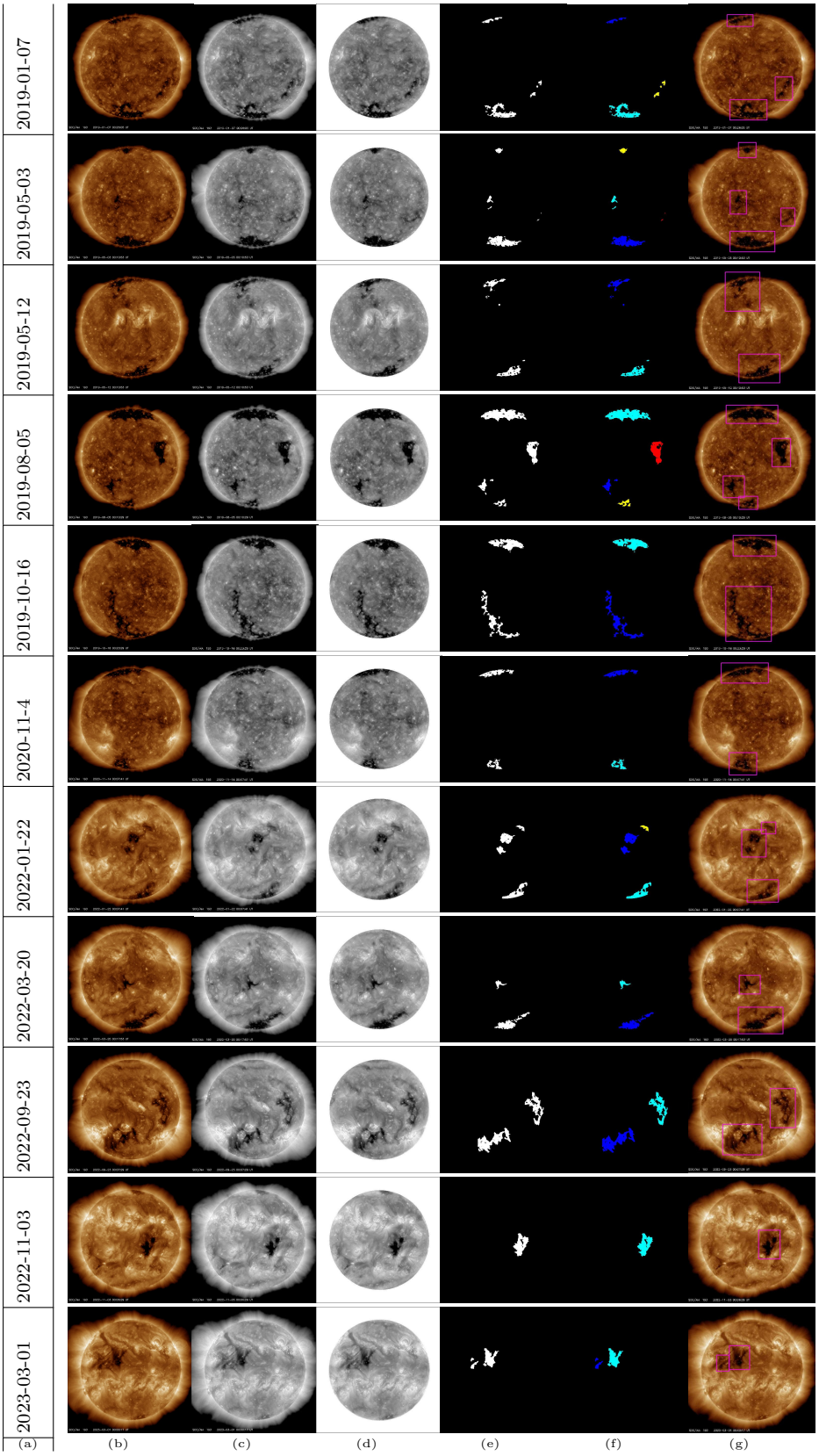

Fig. 3: Stages of the SITDTCCCL method to detect CH regions presented with twelve AIA 193Å images, (a) Dates of collected samples, (b) AIA 193Å images, (c) Converted grayscale images, (d) Segmented solar disk, (e) Supervised Intensity Thresholding, (f) Distance Transform Clustering and Connected Component Labeling, (g) Detected CH regions on AIA 193Å images.

$$\varphi_2 = PT^{\text{neg}}_{-\text{th}}\left[PT1^{+}_{\text{th}}\left(Z^n\right)\right] \equiv \left(\Omega^D \ominus R\right)\oplus R \equiv \Omega^D \circ R, \tag{3}$$

$$\begin{aligned}\varphi_3 = PT^{\text{neg}}_{-2\text{th}}\left[PT1^{+}_{\text{th}}\left(Z^n\right)\right] &\equiv \left(\left(\Omega^D \ominus R\right) \oplus R\right) \oplus R \\ &\equiv \left(\Omega^D \circ R\right) \oplus R,\end{aligned} \tag{4}$$

$$\begin{aligned}\varphi_4 &= PT^{\text{neg}}_{-\text{th}}\left[PT^{\text{pos}}_{2\text{th}}\left[PT1^{-}_{-\text{th}}\left(Z^n\right)\right]\right] \\ &\equiv \left(\left(\left(\Omega^D \oplus R\right) \ominus R\right) \ominus R\right) \oplus R \equiv \left(\Omega^D \bullet R\right) \circ R.\end{aligned} \tag{5}$$

A digital Voronoi tessellation is carried out for the extracted cores. Here, "th" represents the distance map thresholding after PT1, $\circ$ and $\bullet$ symbols identified with opening and closing operations. The index "neg" ("pos") in the transform operation infers $PT1^{-}$ ($PT1^{+}$) transform for the former entity of the distance map after the previous PT, but not the initial image. Possible core of the cluster identified with the aid of final thresholding. The PT2-based clustering can be expressed with respect to the φ_2-based filter in the following Eq. (6):

$$\left(b^{'}\right)\varphi_2^{'} = PT^{\text{neg}}_{x2}\left[PT1^{+}_{x1}\left(Z^n\right)\right]. \tag{6}$$

The threshold value e_i differs from the "th" value. For the opening operation an "adaptive" structuring may be carried out with varying e_i, $(e_1 > 0, e_2 < 0)$ and detect the cluster core having the pixel with cost values $\geq e_1$ (it is the number of non-empty neighbor pixels) and remove the group of pixels having cost values $> e_1$ with $(f(n) + e_2)$ = neighbor in the cost map.

Step 4: Digital space tessellation

A digital Voronoi tessellation is carried out for extracted cores.

Step 5: Data clustering

In the course of tessellation every isolated special pixel is identified with a zone of influence, which implies that the pixel is a member of that specific digital cluster. Initially, every n-dimensional observation belongs to the specific cluster selected for the corresponding digital cubes.

Dispersed CHs regions are grouped through Distance Transform Clustering and every cluster is labeled through connected component labeling because each labeled region is identified as a CH region, providing an efficient means to detect ROI.

In the next step of this work we use the connected component labeling using the algorithm proposed by Di Stefano and Bulgarelli (1999). The working procedure of this classical approach of component labeling is as follows:

Step 1: IMG = binary image, FG = foreground pixels, BG = background pixels, FG and BG are two subsets of IMG. CMP = connected component of IMG, CMP is a subset of FG and all the pixels of CMP are connected.

Step 2: Consider two pixels X and Y as connected if there is a path of pixels $(t_0; t_1 ::: t_n)$ such that $t_o = X$, $t_n = Y$ and $\forall 1 < 1 \leq i \leq nt_{i-1}$ and t_i are neighbors. CMP is 4-connected when it interconnects with 4 surrounding pixels and the CMP is 8-connected when it incorporates 8 neighboring pixels.

Step 3: In IMG, connected components will be identified in the following way: when all pixels belong to a connected component will be assigned a unique label and different components will be identified with some distinguished label values.

Step 4: In the process of labeling background pixels remain unaltered but according to the principle, a new label has to be assigned for them. So, if the image has n number of labels for n connected components, the labeled image must have n+1 labels, the new label l_{BG}, will be assigned to the pixels of BG and other n labels will be used to identify the pixels of n distinct components which belong to FG.

Step 5: It is quite vivid that in the labeled image, labels express the relation among the pixels. The pixels identified with the label l_{BG} are not necessarily connected, but those pixels that bear a label value l_i and $l_i \neq l_{BG}$ are connected and belong to FG.

5. VALIDATION

In this study we used a two-stage validation process to confirm the accuracy of the detected CH regions. Initially, we compared our identified CH regions against visual references from hand-written solar synoptic maps. This validation approach is similar to the method used by Malanushenko and Jones (2005) who validated their detected CH regions against Coronal Hole maps from the National Solar Observatory. The solar synoptic maps used for our validation are accessible at the National Geophysical Data Center (NGDC) of NASA(https://www.ngdc.noaa.gov/). Fig. 4 represents the positional validation of detected CH regions on AIA 193Å images with respect to solar synoptic maps on six different dates. In the second phase of validation, we cross-verified the identified CH regions in the collected images against the CH maps, considered ground truth, obtained from (https://www.spaceweatherlive.com), presented in Fig. 5. This website is a nonprofit organization based in Belgium that provides various reports related to astronomy and solar events. A comparative analysis was conducted between the centroid coordinates and the areas of the detected CH regions in both the AIA (193 Å) images and the CHs maps from Space Weather Live, as presented in Table 1. During the validation process, we allowed a buffer of ±5 pixels for the x and y coordinates of the computed centroid and ±500 pixels for the computation of the detected area. In the comparison section of Table 1, ED represents the

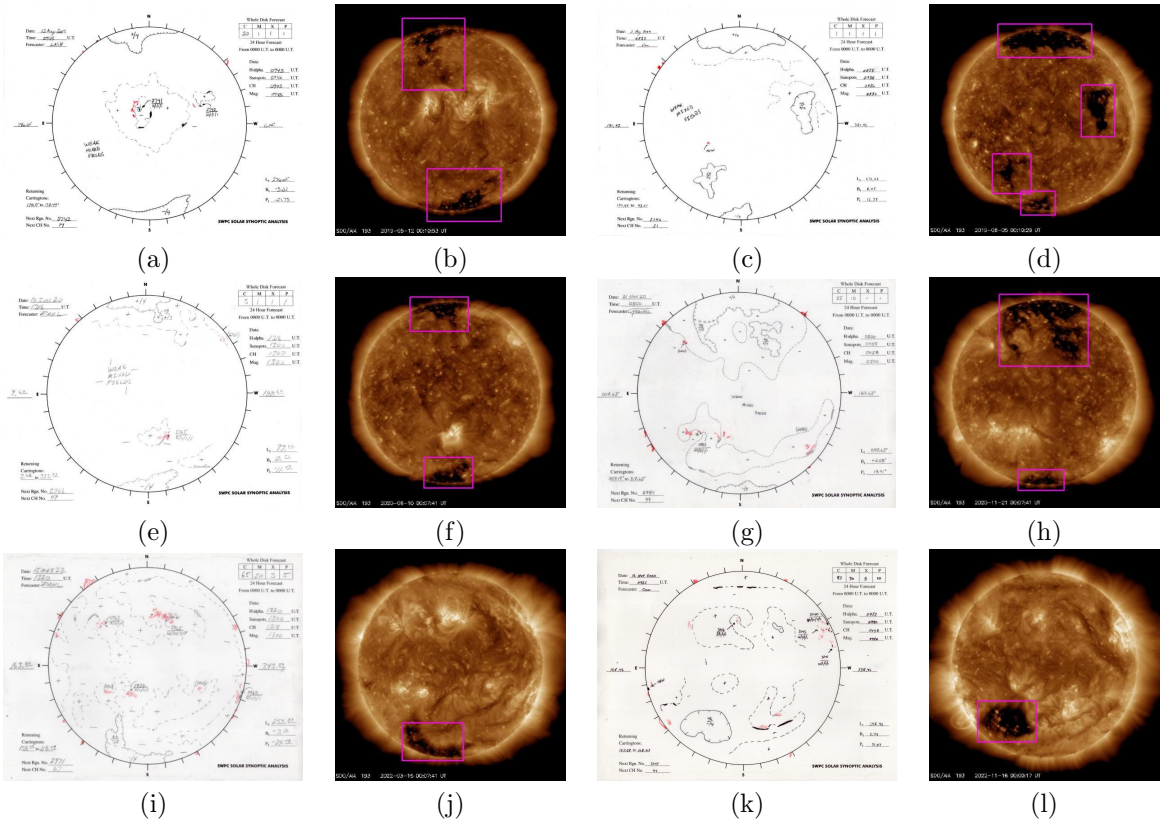

Fig. 4: Positional validation of detected CH regions on AIA 193Å image with respect to solar synoptic map: (a) Solar synoptic map of 2019/05/12; (b) Detected CH regions of 2019/05/12; (c) Solar synoptic map of 2019/08/05; (d) Detected CH regions of 2019/08/05; (e) Solar synoptic map of 2020/06/10; (f) Detected CH regions of 2020/06/10; (g) Solar synoptic map of 2020/11/21; (h) Detected CH regions of 2020/11/21; (i) Solar synoptic map of 2022/03/15; (j) Detected CH regions of 2022/03/15; (k) Solar synoptic map of 2022/11/16; (l) Detected CH regions of 2022/11/16.

Euclidean distance between the centroids of the detected CH region and the centroid of the respective CH region in the CHs map. A represents the area of CH regions in the CHs map of Space Weather Live and B represents the area of CHs regions detected by the proposed method in Table 1. In Fig. 5 (c), (g) and (k) depict the CH regions of the CH map and (b), (f), and (j) present the CH regions detected by the SITDTCCCL method for the dates 2020/06/10, 2022/03/15 and 2022/11/16 respectively. $A \cup B$ represents the CHs area covered by both the CHs map, and the proposed method. It is presented as the entire CH region covered by red, pink and blue, shown in images (d), (h), and (l) of Fig. 5 and also shown in Fig. 6. $A \cap B$ in Table 1 shows the area of intersection between the detected CH region by the SITDTCCCL method and the CH regions of the CH map. Only the pink regions stand for overlapped CH regions, presented in the (d), (h) and (l) images of Fig. 5 and Fig. 6. The greater region of intersection is showing better detection precision of CH regions. In Table 1, BBOX represents the area of the bounding box where the CH regions exist. We also compared the area of detected CH regions (computed) against the area of the CH regions of the CH map (ground truth) on each day of the years 2019, 2020, 2021, and 2022, presented in Fig. 7 (a), (b), (c), and (d), respectively.

6. QUALITATIVE ANALYSIS

In this work, the quality of segmented CHs is assessed using the score of two segmentation matrices namely the Dice coefficient and Jaccard index. The Dice coefficient is represented as (D_c) and the Jaccard index is represented as (J_{In}). We used CH maps of Space Weather Live as ground truth to assess the quality of segmented CH regions. The following equations represent the Dice coefficient and Jaccard index:

$$D_c = \frac{2 \mid A \cap B \mid}{\mid A \mid + \mid B \mid}, \tag{7}$$

$$J_{In} = \frac{D_c}{2 - D_c} = \frac{2 \mid A \cap B \mid}{\mid A \mid + \mid B \mid - \mid A \cap B \mid} = \frac{\mid A \cap B \mid}{\mid A \cup B \mid}. \tag{8}$$

Table 1: Comparative study between the CHs map of Space Weather Live and CH regions detected by SITDTCCCL.

Date	Region	Space Weather Live			SITDTCCCL			Comparison			
		C_x	C_y	Area(A)	C_x	C_y	Area(B)	ED	$A \cup B$	$A \cap B$	BBOX
20190512	1	216.84	76.89	6712	217.00	78.85	6705	1.96	6747	6670	11400
	2	291.36	430.32	7313	289.72	432.42	6926	2.66	7425	6814	12282
20190805	1	184.45	369.26	3552	182.78	369.60	3372	1.70	3935	2989	5183
	2	256.79	84.31	9936	256.64	84.39	9863	0.17	10417	9382	11328
	3	248.00	441.00	2365	246.80	442.01	2301	1.56	3051	1615	3528
	4	376.00	230.00	5565	374.28	229.90	5604	1.72	6064	5105	6900
20200610	1	240.13	77.73	6751	239.08	77.71	6705	1.05	6879	6577	8804
	2	256.60	437.31	5926	256.38	437.10	5831	0.30	6285	5472	6954
20201121	1	269.38	106.67	18359	270.54	105.35	17210	1.76	19184	16384	24288
	2	250.05	450.47	4064	250.10	451.08	3881	0.61	4331	3614	4692
20220315	1	211.14	431.56	5224	210.74	431.45	5118	0.41	5695	4667	9324
20221116	1	175.11	380.55	9426	175.70	380.44	8929	0.60	9544	8811	10750

A represents the total area of the CH regions in the ground truth. B represents the total area of the segmented CH regions using this method.

Tables 2, 3, 4, and 5 contain the (D_c) and Tables 6, 7, 8, 9 contain (J_{In}) of Jan-Mar, April-Jun, July-Sep, Oct-Dec, respectively, from 2019 to 2022.

Table 2: Table of Dice Coefficient(Jan-Mar).

Year	Jan	Feb	Mar
2019	0.9855	0.9931	0.9991
2020	0.9745	0.9965	0.9984
2021	0.9979	0.9969	0.9983
2022	0.8193	0.8587	0.8584

Table 3: Table of Dice Coefficient(April-Jun).

Year	Apr	May	Jun
2019	0.9966	0.9945	0.9896
2020	0.9908	0.9935	0.9850
2021	0.9973	0.9941	0.9955
2022	0.8100	0.7985	0.8265

Table 4: Table of Dice Coefficient(July-Sep).

Year	Jul	Aug	Sep
2019	0.9951	0.9968	0.9948
2020	0.9895	0.9950	0.9892
2021	0.9913	0.9997	0.9967
2022	0.8421	0.8446	0.8642

Table 5: Table of Dice Coefficient(Oct-Dec).

Year	Oct	Nov	Dec
2019	0.9994	0.9983	0.9911
2020	0.9933	0.9862	0.9817
2021	0.9812	0.9627	0.9434
2022	0.8884	0.8385	0.8131

Table 6: Table of Jaccard index (Jan-Mar).

Year	Jan	Feb	Mar
2019	0.9715	0.9864	0.9982
2020	0.9502	0.9931	0.9968
2021	0.9959	0.9938	0.9967
2022	0.6939	0.7524	0.7520

Table 7: Table of Jaccard index (April-Jun).

Year	Apr	May	Jun
2019	0.9933	0.9890	0.9795
2020	0.9818	0.9872	0.9901
2021	0.9947	0.9883	0.9911
2022	0.6806	0.6646	0.7043

Table 8: Table of Jaccard index (July-Sep).

Year	Jul	Aug	Sep
2019	0.9903	0.9937	0.9896
2020	0.9793	0.9901	0.9786
2021	0.9827	0.9995	0.9934
2022	0.7273	0.7311	0.7609

7. OBJECT DETECTION WITH YOLO V8

Object detection comprises two tasks: localization of the object and classification of the image according to the object with the bounding box class of the predicted object Redmon et al. (2015). In this study we have used YOLO v8 which was introduced by Ultralytics in January 2023 Jocher et al. (2023). The anchor-free YOLO v8 architecture has shown fast and

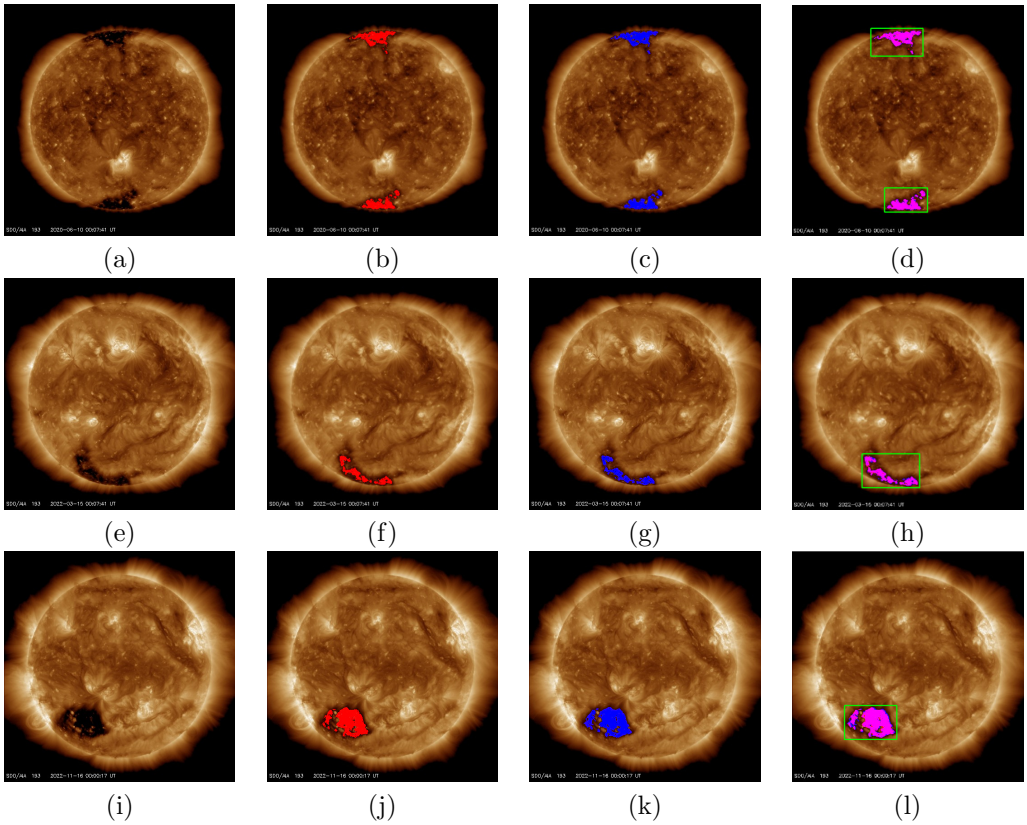

Fig. 5: Validation of detected CH regions in the AIA 193 Å image with respect to the CHs map of Space Weather Live (Ground Truth) : (a) The AIA 193Å image of 2020/06/10, (b) Detected CH regions on 2020/06/10 using the proposed method, (c) The CHs map of 2020/06/10, (d) Overlapped regions between detected CH regions and the CH map on 2020/06/10 (e) The AIA 193 Å image of 2022/03/15, (f) Detected CH regions of 2022/03/15 using the proposed method, (g) The CHs map on 2022/03/15, (h) Overlapped regions between detected CH regions and the CH map on 2022/03/15, (i) The AIA 193Å image of 2022/11/16, (j) Detected CH regions of 2022/11/16 using the proposed method, (k) The CH map on 2022/11/16, (l) Regions of commonality between the detected CH regions and CH map on 2022/11/16.

Table 9: Table of Jaccard index (Oct-Dec).

Year	Oct	Nov	Dec
2019	0.9988	0.9966	0.9823
2020	0.9867	0.9728	0.9642
2021	0.9631	0.9282	0.8929
2022	0.7993	0.7219	0.6851

accurate prediction by decreasing the time taken for NMS through proper optimization of the box prediction. It uses the sigmoid function as the activation function for calculation of the objectness score. Fig. 8 shows the common architecture for YOLO v8 divided into three parts - Backbone, Neck, and Head.

7.1. Backbone

A modified CSPDarknet53 served as the backbone of the YOLOv8 model, which encapsulates the essence of Cross Stage Partial (CSP). The C2f module (2 ConvModule and n BottleNeck) performs the task of feature extraction by integrating the functionalities of the C3 module (3 ConvModule and n BottleNeck) of YOLO v5 and ELAN (Efficient Layer Aggregation Network) Ju and Cai (2023), which was introduced in YOLOv7 Wang et al. (2022). C2f generates rich gradient flow information. A convolutional layer batch normalization and SiLU activation function are integrated with a convmodule.

7.2. Neck

The backbone is coupled with the neck at three different depths (Stage 2, Stage 3 and Stage 4). The neck generates a fusion of features, obtained from various layers of the network and passes that to the Head. It incorporates two special networks, such as the path aggregation network (PAN) Liu et al. (2018) and feature pyramid network (FPN) Lin et al. (2017), to prevent information loss in the course of multiple convolutions.

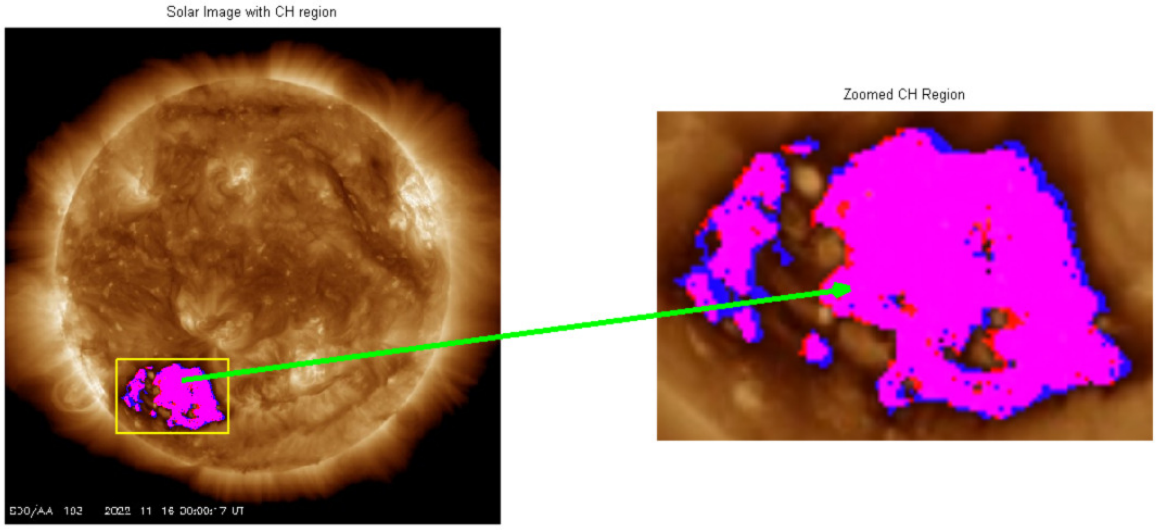

Fig. 6: Enlarged image of the detected CH region on 2022/11/16, showing overlapped region (in pink) between the detected CH region (by SITDTCCCL) and CH map of Space Weather Live.

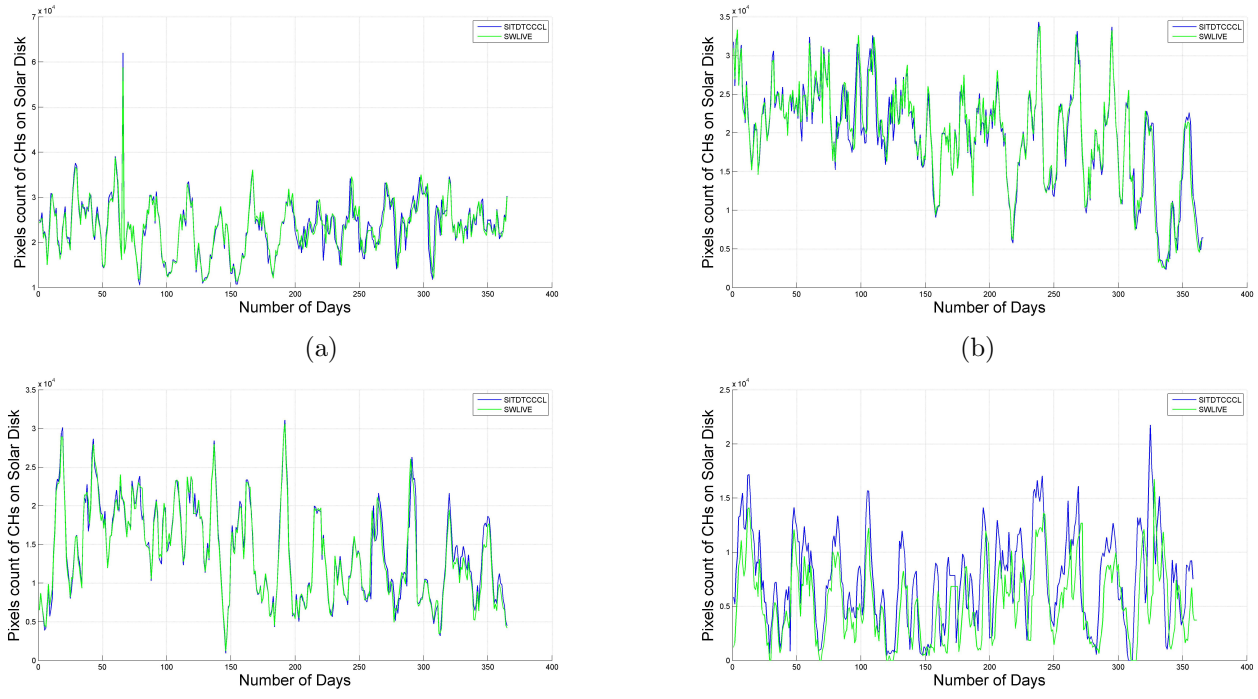

Fig. 7: Day-wise diagrammatic validation of computed area of CH regions in AIA 193Å by SITDTCCCL against the area of CH regions of the CH map of Space Weather Live : (a) Validation of CH regions of the year 2019; (b) Validation of CH regions of the year 2020; (c) Validation of CH regions of the year 2021; (d) Validation of CH regions of the year 2022.

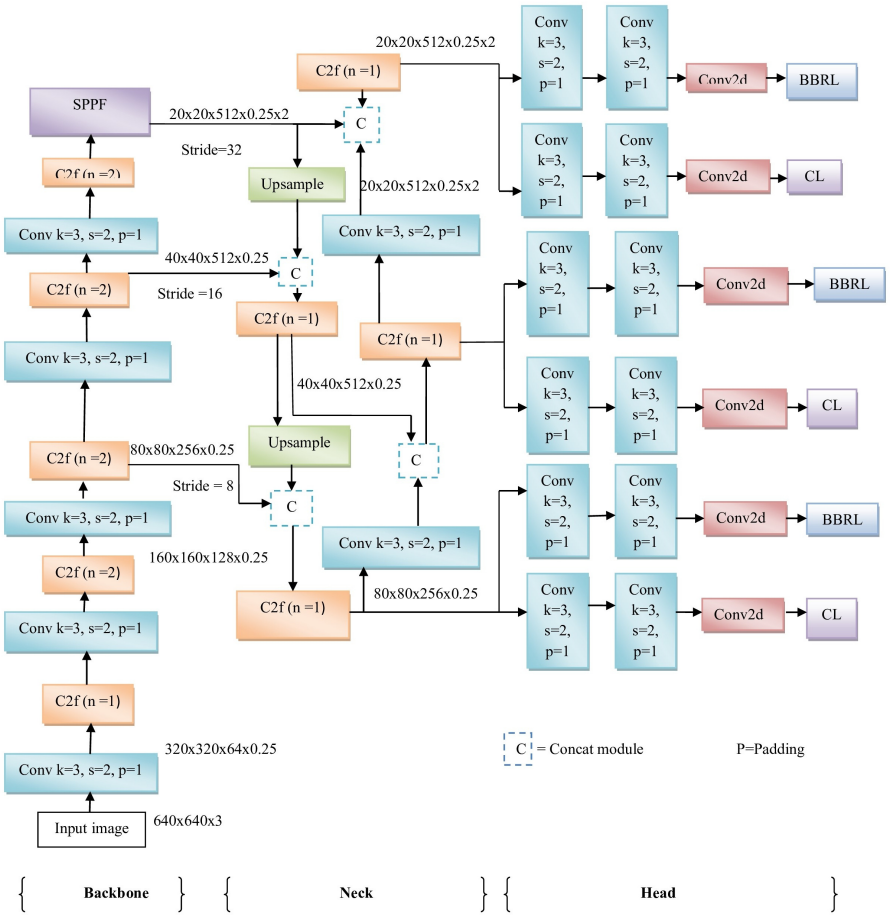

Fig. 8: Architecture of YOLOv8.

7.3. Head

There are three detection heads in the YOLO v8 model. These heads are dedicated to decoupled classification and regression tasks. The decoupled detection Head was introduced by YOLOv6 Terven and Cordova-Esparza (2023) and YOLOX. YOLOv8 is anchor-free because of the decoupled head which helps in the direct prediction of the center of the object and bounding box parameters in Eq. (15). This anchor-free network facilitates the task–aligned one–stage object detection (TOOD).

7.4. Loss function

Loss function represents the loss of information between the ground truth and prediction. It can be represented as an integration of classification and bounding box regression loss as shown in Eq. (13). In YOLO v8 Binary Class Entropy (BCE) the loss can be represented with the Eq. (9):

$$\begin{aligned} \mathrm{BCE}_l = l(x,y) = y_n \cdot \log\log\left(\sigma(x_n+1)\right) \\ + (1-y_n)\cdot \log\log\left(1-\sigma(x_n)\right). \end{aligned} \tag{9}$$

In Eq. (9), n is the number of samples, y_n is the ground truth value, and x_n is the predicted value. The position-based regression loss is presented as sum of Distribution Focal Loss (DFL) and the Complete IoU (CIoU) loss. DFL can be expressed as follows Li et al. (2020):

$$\begin{aligned} \mathrm{DFL}_{S_i,S_{i+1}} = -\big((y_{i+1}-y)\cdot \log\log(S_i) \\ + (y-y_i)\cdot \log\log(S_{i+1})\big), \end{aligned} \tag{10}$$

where y_i represents the left-hand side values of the label y and y_{i+1} represents the right-hand side values of the label y, and where $P\left(y_i\right)$ is computed using the softmax layer denoted by S_i, y is represented in Eq. (11). CIoU loss is presented as the addition of IoU, Distance IoU (DIoU) Zheng et al. (2020), which can be expressed as Eq. (12):

$$y = \sum_{i=0}^{n} P\left(y_i\right).y_i, \tag{11}$$

$$\mathrm{IoU} = \frac{|B \cap B^{gt}|}{|B \cup B^{gt}|}. \tag{12}$$

Where $B_{gt} = (x_{gt}, y_{gt}, w_{gt}, h_{gt})$ is the ground truth and $B = (x, y, w, h)$ is the predicted box.

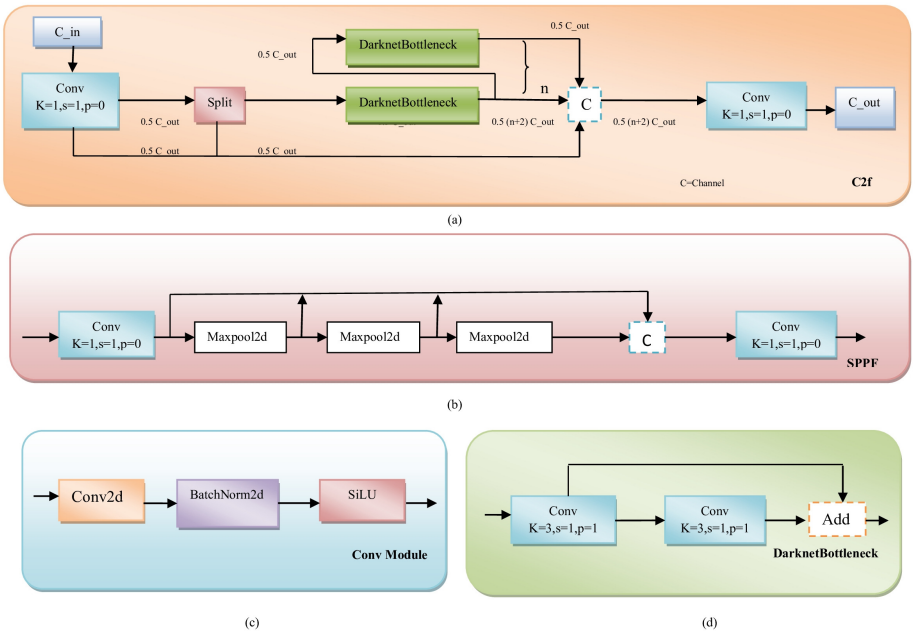

Fig. 9: Sub modules of the YOLOv8 architecture: (a) C2f Module; (b) SPPF Module; (c) Convolution Module; (d) Darknet Bottleneck Module.

$$\text{BBRL} = \text{CIoU}_l = 1 - \text{IoU} + \frac{d^2}{c^2} + \frac{v^2}{1 - \text{IoU} + v}, \quad (13)$$

$$V = \frac{4}{\pi}\left(\arctan\frac{w_{gt}}{w_{ht}} - \arctan\frac{w_p}{h_p}\right)^2, \quad (14)$$

where v is the consistency in aspect ratio with w_{gt} and h_{gt} being the width and height of the ground truth bounding box, w_p and h_p are the width and height of the predicted bounding box; d is the Euclidean distance between the center point of the predicted and ground truth bounding boxes; c is the diagonal length of the smallest box enclosing both boxes Zheng et al. (2020). Finally, the loss function in each decoupled head is expressed as fl, and $\lambda 1$, $\lambda 2$ and $\lambda 3$ are three constants and shown in Eq. (15):

$$fl = \lambda 1\ \text{BCE}l + \lambda 2\ \text{DFL} + \lambda 3\ \text{BBRL}. \quad (15)$$

7.5. AdamW optimization

The AdamW optimization is a stochastic optimization method for the decoupled weight decay regularization method introduced by Loshchilov and Hutter (2017), which can be expressed using the following Eq. (16). g_t is the gradiant at time t, $\nabla f(\theta_t)$ batch gradiant at time t, w_t decay rate, and θ_t is decay at time t.We used the AdamW optimization in this experiment in training of YOLO v8 models. We deployed three YOLOv8 models, such as YOLO v8n (nano), YOLOv8m (medium), and YOLOv8x (extra large) for our experiment and studied their comparative performance in the detection of the CH regions:

$$g_t = \nabla f(\theta_t + w_t\theta_t). \quad (16)$$

8. EXPERIMENT AND RESULTS

In this experiment, we used 1672 images, 111 images with no CH regions, and 1561 images with the CH regions. In this data set, 85% data were used in training and validation, and 15% data were used in the testing process. We have created annotation files according to Microsoft's COCO data set format. We deployed three models of YOLO v8, such as YOLO v8n (nano), YOLO v8m (medium), and YOLO v8x (extra large) for automatic detection of the CH regions. We continued the training and testing process from epoch 1 to 40 for each YOLO v8 model. YOLO v8n contains 168 layers, 3006038 parameters, 8.1 GFLOPs, and takes 0.286 hours to complete 40 epochs. YOLO v8m comprises 218 layers, 25840918 parameters, 78.7 GFLOPs, which finishes 40 epochs in 0.466 hours. YOLO v8x is the largest among the YOLO v8 models, which incorporates 268 layers, 68125494 parameters, 257.4 GFLOPs, and completes 40 epochs in 1.076 hours. We used four evaluation matrices for this work, namely, F1 score, Precision (P), Recall (R), and mean Average Precision (mAP), which are defined later. The following Fig. 8 presents the automatically detected CHs on twelve different days (2019/04/12, 2021/07/29, 2021/08/27, 2021/08/28, 2021/08/30, 2021/09/07, 2021/10/16, 2021/10/29, 2021/11/30, 2021/12/15, 2022/11/16, and 2023/06/27) of the transition phase between the 24th and 25th solar cycle. It also incorporates four terms required for these evaluation matrices, such as True Positive (TP), when the predicted object matches its label with the ground truth, it is said that the model has identified the object correctly. True Negative (TN) occurs when the predicted label

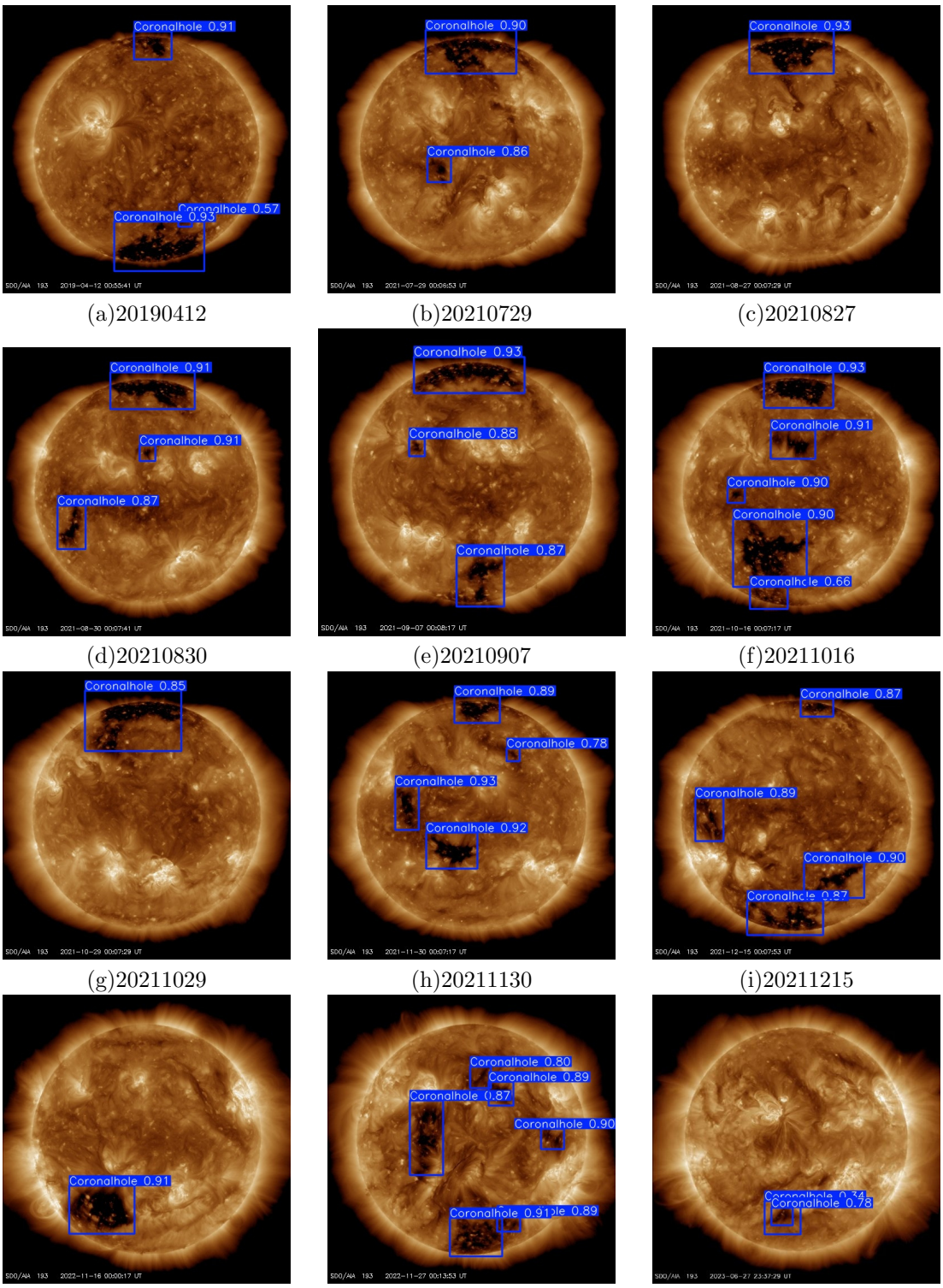

Fig. 10: Automatic detection of CH regions by YOLOv8x on different dates.

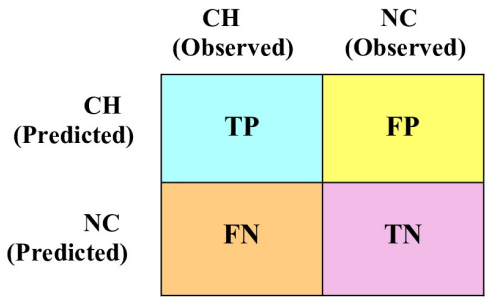

Fig. 11: Coronal Hole (CH) and Not Coronal Hole (NC) classification contingency (Confusion Matrix).

of the object differs from the ground truth, or the model has identified the object in the wrong class. False Positive (FP) is when a model labels an object, but the label does not belong to the ground truth, which means such an object is detected that is not there, or wrongly labeled. False Negative (FN) occurs when a label is not predicted by the model, which means the object is not being identified properly. In this work, either the solar disk has one or more CH regions and is labeled as CH, or the solar disk has no CH regions on it, then we label it as NC, meaning "No CH".

Precision of a class is also termed as a positive predicted value because it is a ratio of true positives (TP) and the total number of predicted positives can be expressed with Eq. (17):

$$\text{Precision} = \frac{\text{TP}}{\text{TP} + \text{FP}}. \tag{17}$$

Recall is synonymous with true positive rate (TPR) or sensitivity, as it can be defined as the ratio of TP and total ground truth positives in the following way:

$$\text{Recall} = \frac{\text{TP}}{\text{TP} + \text{FN}}. \tag{18}$$

The F1 score can be expressed in terms of Precision and Recall. In the field of computer vision and Data Science, the F1 score is also defined as harmonic mean of Precision and Recall:

$$\text{F1 score} = 2 \times \frac{\text{Precisson} \times \text{Recall}}{\text{Precisson} + \text{Recall}}. \tag{19}$$

For evaluation of the object detection task, mAP is widely used, which also includes the precision-recall (PR) area under the curve (AUC) and IoU (based on the Jaccard overlap) between the bounding boxes of our dataset and predicted boxes is greater than 0.5. The mAP can be expressed using Eq. (20) where AP_i is the average precision of each class and N is the total number of classes, including the background as a class type:

$$\text{mAP} = \frac{1}{N} \sum_{i=1}^{N} AP_i. \tag{20}$$

In this study we have performed training and testing on the three different YOLOv8 models and evaluated their performance for the four discussed matrices. Their respective accuracy of object detection is presented in tables below. Table 10 contains values of the F1 score, Precision, Recall, and mAP values

Table 10: Performance table of YOLOv8n.

No of Epoch	F1 Score	Precision	mAP50	Recall
1	**0.84**	**0.917**	**0.883**	0.98
2	0.86	0.949	0.894	**0.97**
3	0.84	0.997	**0.883**	0.98
4	0.86	0.944	0.916	0.98
5	0.85	0.954	0.899	0.98
6	0.85	0.983	0.895	0.98
7	0.88	0.967	0.927	0.99
8	0.87	0.972	0.927	0.99
9	0.86	0.932	0.913	0.99
10	0.90	0.929	0.931	0.98
11	0.89	**0.978**	0.935	0.99
12	0.88	0.935	0.931	0.99
13	0.87	0.947	0.910	0.99
14	0.88	0.909	0.933	0.99
15	0.87	0.919	0.933	0.98
16	0.90	0.926	0.947	0.99
17	0.89	0.932	0.952	0.99
18	0.91	0.925	0.961	0.99
19	0.89	0.956	0.935	0.99
20	0.89	0.923	0.947	0.99
21	0.88	**0.917**	0.927	0.99
22	0.89	0.917	0.953	0.99
23	0.91	0.919	0.956	0.99
24	0.89	0.949	0.935	0.99
25	0.90	0.938	0.956	**0.99**
26	0.91	0.941	0.964	0.99
27	0.89	0.968	0.940	0.99
28	0.90	0.942	0.956	0.99
29	0.89	0.933	0.942	0.99
30	0.89	0.964	0.948	0.99
31	0.90	0.935	0.948	0.99
32	0.91	0.944	0.960	0.99
33	0.89	0.934	0.946	0.99
34	0.90	0.917	0.962	0.99
35	0.91	0.929	0.959	0.99
36	**0.93**	0.969	**0.965**	0.99
37	0.92	0.971	0.962	0.99
38	0.91	0.948	0.956	0.99
39	0.89	0.935	0.947	0.99
40	0.92	0.956	**0.965**	0.99

for Epochs 1 to 40 for YOLOv8n, similarly Table 11 for YOLOv8m, and Table 12 for YOLOv8x. Automatic detection of the CH regions using a deep learning technique has been done as a part of the solar event Kucuk et al. (2017b), Baek et al. (2021). Still, those models used cropped images and labeled images of multiple AIA images of different wavelengths instead of automatic detection of the CH regions and have shown less accuracy in terms of detection of the CH regions. Kucuk et al. (2017a) have shown the detection rate 77% (TPR or Recall) and Baek et al. (2021) got 77%(mAP) and 76%(mAP) for Faster RCN and SSD, respectively and TPR score 83% and 85% for Faster RCN and SSD.

Table 11: Performance table of YOLOv8m.

No of Epoch	F1 Score	Precision	mAP50	Recall
1	**0.85**	0.947	0.893	**0.97**
2	0.86	0.926	0.905	0.98
3	0.86	0.930	0.907	0.97
4	0.85	0.886	**0.874**	0.98
5	0.89	**0.847**	0.933	0.98
6	0.87	0.872	0.928	0.98
7	0.88	0.910	0.927	0.98
8	0.90	0.884	0.937	0.98
9	0.89	0.913	0.935	0.98
10	0.90	0.896	0.936	**0.99**
11	0.89	0.913	0.924	0.98
12	0.89	0.938	0.932	0.99
13	0.89	0.935	0.937	0.99
14	0.90	0.926	0.951	0.99
15	0.89	0.893	0.945	0.98
16	0.89	0.904	0.931	0.98
17	0.91	0.914	0.952	0.99
18	0.92	0.943	0.967	0.99
19	0.92	0.949	0.973	0.99
20	0.93	0.906	0.971	0.99
21	0.91	0.910	0.910	0.98
22	0.92	0.952	0.966	0.99
23	0.93	0.927	0.974	0.99
24	0.94	0.952	0.972	0.99
25	0.94	0.946	0.975	0.99
26	0.90	0.914	0.946	0.98
27	0.93	0.920	0.974	0.99
28	0.94	0.947	0.975	0.99
29	0.94	0.952	0.973	0.99
30	0.91	0.949	0.961	0.99
31	0.92	0.927	0.956	0.98
32	0.94	0.949	0.972	0.99
33	0.94	0.946	0.972	0.99
34	0.94	0.966	0.975	0.99
35	0.92	0.968	0.967	0.99
36	0.93	**0.961**	0.965	0.99
37	0.93	0.935	0.967	0.99
38	0.94	0.946	0.971	0.99
39	**0.95**	0.960	0.973	0.99
40	0.94	0.956	**0.977**	0.99

Table 12: Performance table of YOLOv8x.

No of Epoch	F1 Score	Precision	mAP50	Recall
1	0.90	0.934	0.947	0.99
2	0.91	0.926	0.955	0.99
3	0.90	**0.877**	0.956	0.99
4	0.90	0.877	0.956	0.99
5	0.85	0.966	0.893	**0.97**
6	**0.84**	0.944	**0.887**	0.98
7	0.87	0.931	0.910	0.99
8	0.93	0.928	0.970	**1.00**
9	0.85	0.90	0.904	0.98
10	0.87	0.879	0.908	0.98
11	0.87	0.896	0.906	0.98
12	0.89	0.917	0.932	0.98
13	0.91	0.882	0.956	0.99
14	0.89	0.928	0.927	0.98
15	0.88	0.896	0.930	0.99
16	0.89	0.859	0.943	0.99
17	0.88	0.898	0.918	0.99
18	0.90	0.893	0.950	0.99
19	0.92	0.901	0.967	0.99
20	0.90	0.90	0.949	0.99
21	0.90	0.914	0.951	0.99
22	0.92	0.891	0.967	0.99
23	0.90	0.922	0.951	0.99
24	0.91	0.884	0.956	0.99
25	0.92	0.922	0.969	0.99
26	0.92	0.917	0.962	0.99
27	0.90	0.906	0.955	0.99
28	0.90	0.893	0.951	0.99
29	0.91	0.916	0.963	0.99
30	0.93	0.942	0.975	0.99
31	0.91	0.929	0.965	0.99
32	0.93	0.947	0.969	0.99
33	0.91	0.918	0.964	0.99
34	0.90	0.927	0.951	0.99
35	0.93	0.947	0.971	0.99
36	0.91	0.948	0.958	0.99
37	0.93	0.923	0.973	0.99
38	0.94	0.942	0.977	**1.00**
39	0.92	**0.952**	0.968	0.99
40	**0.95**	0.946	**0.981**	**1.00**

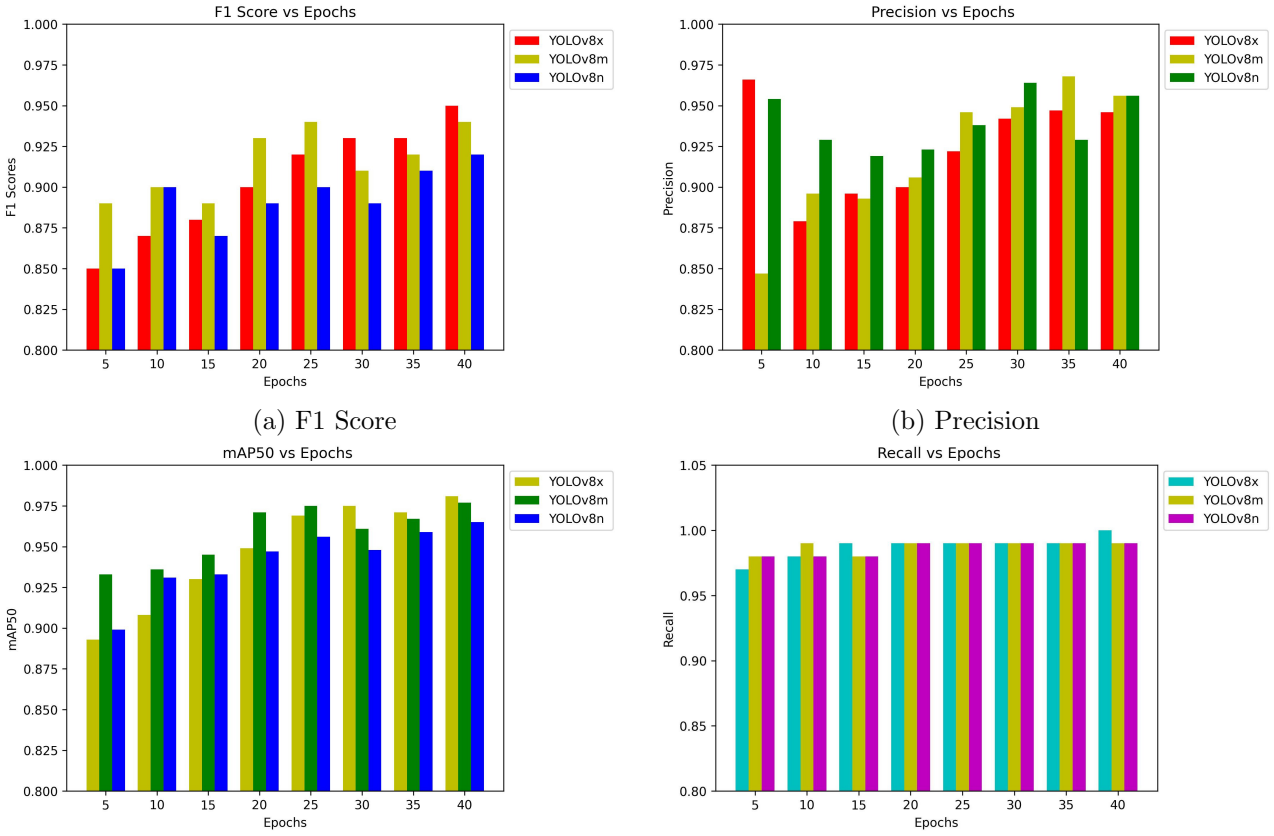

(a) F1 Score (b) Precision

(c) mAP (d) Recall

Fig. 12: Comparison of various evaluation parameters with YOLOv8n, YOLOv8m and YOLOv8x in different Epochs.

A successful comparison has been drawn here. It has been found that the recall value of the research outcome is confined within the range of 0.97 to 1.00, the obtained F1 score stays in $0.84 > F1 > 0.92$, maximum F1 score is 0.92 for YOLOv8n at epoch 40, the precision belongs to the range started from 0.917 to be 0.978, its maximum value is found 0.978 at epoch 11, as for mAP50, it stays in the range between 0.894 to 0.965, and has maximum 0.965 at epoch 40. In the case of YOLOv8m, F1 is confined within the range of 0.85 to 0.95 and we get the highest F1 score 0.95 at epoch 39, the value of Precision is confined within the range of 0.847 to 0.961, the maximum Precision is 0.961 at epoch 36, the value of mAP50 stays in $0.874 < mAP50 < 0.977$, the highest mAP50 is 0.977 at epoch 40. The outcome of the recall value ranges between 0.98 and 0.99, whereas the maximum recall value is at epoch 10. For the YOLOv8x model, the F1 score confined 0.84 to 0.95 and we get the highest F1 score of 0.95, at epoch 40, Precision stays in $0.877 < Precision < 0.952$, its maximum 0.952 at epoch 39. As for mAP50, it stays in the range between 0.887 and 0.981, and has maximum 0.981 at epoch 40. The following Table 10, Table 11 and Table 12 contain the epoch-wise performance scores of the F1 score, Precision, mAP50, and Recall (True Positive Rate) of YOLOv8n (nano), YOLOv8m (medium), YOLOv8x (extra large), respectively.

9. DISCUSSION

In this experiment, we used three YOLOv8 models, namely YOLOv8n, YOLOv8m and YOLOv8x for automated detection of coronal hole (CH) regions, analyzing and comparing their performance in this task. While Kucuk et al. (2017a), Baek et al. (2021) used nearly 10,000 data points for the CH region detection, our study used only 1561 images for training, testing and validation, achieving superior accuracy in the CH region identification. Our proposed model demonstrated impressive results with the YOLOv8n (nano) architecture, achieving 93% (F1 score), 97.1% (Precision), 96.5% (mAP), and 99% (True Positive Rate) accuracy in the CH region identification. The YOLOv8m (medium) architecture exhibited accuracy rates of 95%, 96.1%, 97.7%, and 99% for the F1 score, Precision, mAP, and TPR, respectively. The YOLOv8x (extra-large) network architecture demonstrated the highest accuracy in the CH region detection, achieving rates of 95% for the F1 score, 95.2% for Precision, 98.1% for mAP, and 100% for Recall. Given that the 193 Å

wavelength includes the activere gions, quiet sun, and CH regions, we intend to classify these regions in the future. Additionally, we aim to classify the CH regions based on their positions and locations. Recognizing the portrayal of CH regions as solar events in various works, we envision automated detection of solar events such as sunspots, solar flares, ARs, solar prominences, and coronal mass ejections. In the future, we plan to implement the YOLO-NAS network architecture for the CH region detection.

Acknowledgements – We want to thank Dr. Sourav Samanta for giving his valuable suggestions for our experiment. We are also deeply grateful to the scientists who are associated with the Solar Dynamic Observatory for providing 193Å AIA images to pursue this research.

REFERENCES

Altschuler, M. D., Trotter, D. E. and Orrall, F. Q. 1972, SoPh, 26, 354
Antonucci, E., Dodero, M. A., Giordano, S., Krishnakumar, V. and Noci, G. 2004, A&A, 416, 749
Armstrong, J. A. and Fletcher, L. 2019, SoPh, 294, 80
Baek, J.-H., Kim, S., Choi, S., et al. 2021, SoPh, 296, 160
Bandyopadhyay, S., Das, S. and Datta, A. 2020, AdSpR, 65, 2435
Barra, V., Delouille, V., Kretzschmar, M. and Hochedez, J.-F. 2009, A&A, 505, 361
Bochkovskiy, A., Wang, C.-Y. and Liao, H.-Y. M. 2020, arXiv:2004.10934
Boucheron, L. E., Valluri, M. and McAteer, R. T. J. 2016, SoPh, 291, 2353
Cai, Z. and Vasconcelos, N. 2018, in 2018 IEEE/CVF Conference on Computer Vision and Pattern Recognition (IEEE)
Caplan, R. M., Downs, C. and Linker, J. A. 2016, ApJ, 823, 53
Ciecholewski, M. 2015, Journal of Visual Communication and Image Representation, 33, 203
Colak, T. and Qahwaji, R. 2013, SoPh, 283, 143
Cranmer, S. R. 2009, Living Reviews in Solar Physics, 6, 3
Dai, J., Li, Y., He, K. and Sun, J. 2016, arXiv:1605.06409
de Toma, G. 2011, SoPh, 274, 195
De Wit, T. D. 2006, SoPh, 239, 519
Delaboudinière, J.-P., Artzner, G. E., Brunaud, J., et al. 1995, SoPh, 162, 291
Di Stefano, L. and Bulgarelli, A. 1999, in 10th International Conference on Image Analysis and Processing, 1
Ervin, T., Advisor: Bortnik, J. D. 2021, Coronal Hole Detection using Machine Learning Techniques
Garton, T. M., Gallagher, P. T. and Murray, S. A. 2018, Journal of Space Weather and Space Climate, 8, A02
Girshick, R., Donahue, J., Darrell, T. and Malik, J. 2014, in 2014 IEEE Conference on Computer Vision and Pattern Recognition (IEEE)
Gopalswamy, N., Mäkelä, P., Xie, H., Akiyama, S. and Yashiro, S. 2009, Journal of Geophysical Research (Space Physics), 114, A00A22
Gosling, J. T. and Pizzo, V. J. 1999, SSRv, 89, 21
Harvey, K. L. and Recely, F. 2002, SoPh, 211, 31
Hassler, D. M., Dammasch, I. E., Lemaire, P., et al. 1999, Sci, 283, 810
He, K., Gkioxari, G., Dollar, P. and Girshick, R. 2017, in 2017 IEEE International Conference on Computer Vision (ICCV) (IEEE)
Henney, C. J. and Harvey, J. W. 2007, arXiv:0701122
Huang, J., Rathod, V., Sun, C., et al. 2017, in Proceedings of the IEEE conference on computer vision and pattern recognition, 7310
Illarionov, E., Kosovichev, A. and Tlatov, A. 2020, ApJ, 903, 115
Illarionov, E. A. and Tlatov, A. G. 2018, MNRAS, 481, 5014
Jarolim, R., Veronig, A. M., Hofmeister, S., et al. 2021, A&A, 652, A13
Jocher, G., Stoken, A., Borovec, J., et al. 2020, ultralytics/yolov5: v3.1 - Bug Fixes and Performance Improvements
Jocher, G., Chaurasia, A. and Qiu, J. 2023, Ultralytics YOLOv8
Ju, R.-Y. and Cai, W. 2023, arXiv:2304.05071
Kirk, M. S., Pesnell, W. D., Young, C. A. and Hess Webber, S. A. 2009, SoPh, 257, 99
Krieger, A. S., Timothy, A. F. and Roelof, E. C. 1973, SoPh, 29, 505
Krista, L. D. and Gallagher, P. T. 2009, SoPh, 256, 87
Kucuk, A., Aydin, B. and Angryk, R. 2017a, in 2017 IEEE International Conference on Big Data (Big Data) (IEEE)
Kucuk, A., Banda, J. M. and Angryk, R. A. 2017b, Solar Event Classification Using Deep Convolutional Neural Networks (Springer International Publishing), 118
Lakhina, G. S. and Tsurutani, B. T. 2016, Geoscience Letters, 3, 5
Lemen, J. R., Title, A. M., Akin, D. J., et al. 2012, SoPh, 275, 17
Li, C., Li, L., Jiang, H., et al. 2022, arXiv:2209.02976
Li, X., Wang, W., Wu, L., et al. 2020, arXiv:2006.04388
Lin, T.-Y., Maire, M., Belongie, S., et al. 2014, Microsoft COCO: Common Objects in Context (Springer International Publishing), 740
Lin, T.-Y., Dollár, P., Girshick, R., et al. 2016, arXiv:1612.03144
Lin, T.-Y., Dollar, P., Girshick, R., et al. 2017, in Proceedings of the IEEE Conference on Computer Vision and Pattern Recognition (CVPR)
Liu, S., Qi, L., Qin, H., Shi, J. and Jia, J. 2018, arXiv:1803.01534
Loshchilov, I. and Hutter, F. 2017, arXiv:1711.05101
Lowder, C., Qiu, J. and Leamon, R. 2017, SoPh, 292, 18
Malanushenko, O. V. and Jones, H. P. 2005, SoPh, 226, 3
Odstrčil, D. and Pizzo, V. J. 1999, JGR, 104, 483
Pesnell, W. D., Thompson, B. J. and Chamberlin, P. C.

2012, SoPh, 275, 3
Qahwaji, R. and Colak, T. 2007, SoPh, 241, 195
Redmon, J. and Farhadi, A. 2017, in 2017 IEEE Conference on Computer Vision and Pattern Recognition (CVPR) (IEEE)
Redmon, J. and Farhadi, A. 2018, arXiv:1804.02767
Redmon, J., Divvala, S., Girshick, R. and Farhadi, A. 2015, arXiv:1506.02640
Ren, S., He, K., Girshick, R. and Sun, J. 2017, IEEE Transactions on Pattern Analysis and Machine Intelligence, 39, 1137
Robbins, S., Henney, C. J. and Harvey, J. W. 2006, SoPh, 233, 265
Rotter, T., Veronig, A. M., Temmer, M. and Vršnak, B. 2015, SoPh, 290, 1355
Scherrer, P. H., Bogart, R. S., Bush, R. I., et al. 1995, SoPh, 162, 129
Scherrer, P. H., Schou, J., Bush, R. I., et al. 2012, SoPh, 275, 207
Scholl, I. F. and Habbal, S. R. 2008, SoPh, 248, 425
Schou, J., Scherrer, P. H., Bush, R. I., et al. 2012, SoPh, 275, 229
Sheeley, Jr., N. R. and Wang, Y.-M. 2002, Apj, 579, 874
Starovoitov, V. 1996, Pattern Recognition Letters, 17, 231
Terven, J. and Cordova-Esparza, D. 2023, arXiv:2304.00501
Verbeeck, C., Delouille, V., Mampaey, B. and De Visscher, R. 2014, A&A, 561, A29
Vršnak, B., Temmer, M. and Veronig, A. M. 2007, SoPh, 240, 315
Wang, C.-Y., Bochkovskiy, A. and Liao, H.-Y. M. 2022, arXiv:2207.02696
Wang, Y.-M., Hawley, S. H. and Sheeley, Jr., N. R. 1996, Sci, 271, 464
Wilhelm, K. 2006, A&A, 455, 697
Woods, T. N., Eparvier, F. G., Hock, R., et al. 2012, SoPh, 275, 115
Zheng, Z., Wang, P., Liu, W., et al. 2020, Proceedings of the AAAI Conference on Artificial Intelligence, 34, 12993

АУТОМАТСКА ДЕТЕКЦИЈА ВИСОКЕ ТАЧНОСТИ ЗА КОРОНАЛНЕ РУПЕ ОД ЈАНУАРА 2019. ДО ЈУЛА 2023. ГОДИНЕ КОРИСТЕЋИ ПОДАТКЕ AIA НА 193 АНГСТРЕМА ДОБИЈЕНЕ НА СОЛАРНОЈ ДИНАМИЧКОЈ ОПСЕРВАТОРИЈИ

Dibyadeep Nandi[1], **Soumya Roy**[2], **Amrita Prasad**[3] and **Sankar Narayan Patra**[1]

[1] *Department of Instrumentation & Electronics Engineering, Jadavpur University, India*
E–mail: *dibyadeep.nandi@gmail.com, sankar.n.patra@gmail.com*

[2] *Department of Applied Electronics & Instrumentation Engineering, Haldia Institute of Technology, MAKAUT, India*

[3] *Department of Data Science, Cardiff School of Technologies, Cardiff Metropolitan University, United Kingdom*

УДК 523.98 : 004.932 : 52–44
Оригинални научни рад

Коронални рупе имају важну улогу у соларној физици. Оне доприносе настанку геомагнетних олуја. Емисија наелектрисаних честица у међупланетарни простор утиче на свемирске временске прилике. Коронални рупе као значајан део Сунчеве активности, имају велики утицај на климу Земље. Због тога је откривање коронални рупа значајан задатак и већ је било доста покушаја у том правцу. У овом раду предлажемо нови метод за аутоматско откривање региона коронални рупа коришћењем технике дубоког учења. Користили смо методу надгледаног одређивања прага интензитета са груписањем трансформације растојања и означавањем повезаних компоненти (енг. *Supervised Intensity Thresholding with Distance Transform Clustering and Connected Component Labeling*, SITDTCCCL) ради проналажења региона од интереса на снимцима таласне дужине 193 Å прикупљеним са Соларне динамичке опсерваторије (енг. SDO). Савремени метод дубоког учења (YOLO v8) показао је изузетне резултате у откривању коронални рупа са вредностима показатеља као што су F1 резултат 95%, прецизност 97, 1%, мера тачности у детекцији објеката (енг. mAP50) 98, 1% и стопе истински позитивних резултата (енг. TPR) 100%.